AKARI/IRC All-Sky Survey Point Source Catalogue Version 1.0
– Release Note (Rev.1) –

AKARI/IRC Team
Prepared by H. Kataza [1], C. Alfageme [2], A. Cassatella [2], N. Cox [2], H. Fujiwara [3], D. Ishihara [4], S. Oyabu [1], A. Salama [2], S. Takita [1], I. Yamamura [1]

Version 1.0, March 30, 2010

Abstract

The AKARI/IRC Point Source Catalogue Version 1.0 provides positions and fluxes of 870,973 sources (844,649 sources in 9μm band and 194,551 sources in 18μm band) in the Mid-Infrared wavelengths. This document describes the outline of the data processing and calibration, and basic performance of the released catalogue. The users of the catalogue are requested to read this document carefully before critical discussions with the data.

Any questions and comments are appreciated via ISAS Helpdesk *iris_help@ir.isas.jaxa.jp*.

Update history		
2010/03/30		Document Version 1.0 release.

Contents

---

[1] ISAS/JAXA
[2] ESAC/ESA
[3] Tokyo Univ.
[4] Nagoya Univ.

1 Overview

1.1 The AKARI All-Sky Survey

The Infrared Astronomical Satellite AKARI (Murakami et al. 2007) was launched on February 21st, 2006 (UT). After three weeks of performance verification phase (PV) (April 13th to May 7th), Phase 1 observation started on the May 8th and continued until November 9th, followed by Phase 2 observation until the exhaustion of liquid Helium on the August 26th, 2007. One of the main missions of AKARI is to carry out the All-Sky Survey in four photometric bands in the far-infrared wavelengths in 50μm -180μm range with the Far-Infrared Surveyor (FIS; Kawada et al. 2007), and in two mid-infrared bands with effective wavelength at 9 and 18 μm with the Infrared Camera (IRC; Onaka et al. 2007). The All-Sky Survey had the highest priority in Phase 1 operations. In Phase 2 the observation plan was highly optimized for the FIS survey (not for the IRC survey) to fill the scan gaps caused in Phase 1 under constraints of carrying out the maximum number of pointed observations. As the result the IRC scanned 96 / 97 percent [5] of the entire sky in 9 / 18 μm band twice or more during the 16 months of the cryogenic mission phase.

The primary product from the survey is the point source catalogue that we describe in this document. It is regarded as the primary catalogue from the AKARI IRC survey. The catalogue is supposed to have a uniform detection limit over the entire sky, based on the uniform source detection limit per scan observation. Redundant observations are used to increase the reliability of the detection.

1.2 The Infrared Camera All-Sky Survey

The Infrared Camera All-Sky Survey (Ishihara et al. 2010) has been done by two channel of the Infrared Camera (IRC): MIR-S channel and MIR-L channel. The specifications of the two channels are summarized in Table1. MIR-L has a field of view at about 20 arcminutes away from that of MIR-S. Photometric bands used for the All-Sky Survey are S9W (6.7 – 11.6 μm; MIR-S) with the effective wavelength at 9 μm and L18W (13.9 – 25.6 μm; MIR-L) with the effective wavelength at 18 μm. Figure 1 shows the relative spectral response (link to the data exists in "AKARI Observers Page" *http://www.ir.isas.jaxa.jp/ASTRO-F/Observation/*, see also AKARI IRC Data User Manual v1.4) for both bands.

Table 1: IRC MIR-S and MIR-L Specification

	MIR-S	MIR-L
Camera Field of View (arcmin)	$10' \times 9'.6$	$10'.7 \times 10'.2$
Pixel scale (arcsec)	$2''.34 \times 2''.34$	$2''.51 \times 2''.39$
Band for All-Sky Survey	S9W	L18W
Effective wavelength	9μm	18μm
FWHM (arcsec)	$5''.5$	$5''.7$
Virtual pixel size (arcsec)	$9''.36 \times 9''.36$	$10''.4 \times 9''.36$
Detector	Si:As/CRC-744 (256 × 256)	
Conversion factor	$\sim 6e^-/ADU$	
Dark current	$< 30e^-/sec$	

FOVs and scales are formatted as cross-scan × in-scan.

---

[5] FIS scanned area is about 94% .

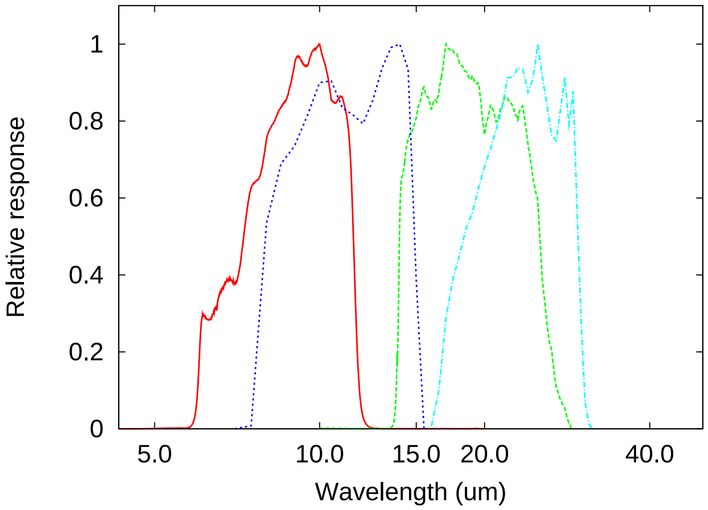

Figure 1: Relative spectral response curve of the S9W (red solid curve) and L18W bands (green dashed) in units of electron/energy normalized to the peak. The system response curves of the IRAS 12 μm (blue dotted) and 25 μm bands (cyan dashed-dotted) are also shown for comparison. The RSRs of the IRC are available at *http://www.ir.isas.jaxa.jp/ASTRO-F/Observation/RSRF/IRC_FAD/index.html*. The system response curves of the IRAS are taken from Table II.C.5 of IRAS Explanatory Supplement (Beichman et al. 1988).

A special read-out operating mode has been adopted for the All-Sky Survey observations (Ishihara et al. 2006). In this mode, pixels in 16 rows (Y=113 to 128) of total 256 rows are selected to output the signal and only the data from pixels in 2 rows (Y=117 and 125) are taken for the observation. Other pixels are not selected individually to shorten the sampling period. For each used pixel, the output signal is sampled 306 times non-destructively, and the pixel is reset. The row direction corresponds to the cross-scan direction. The scan speed is about 215 arcsec/sec and the sampling period of the output signal is 44 ms. Integration time at a point on sky is determined by the pixel field of view and scan speed, whereas spatial sampling in the scan direction is determined by the sampling rate and scan speed. The data of every four adjacent pixels are binned together (added and 2 bit-shifted to divide by four). In this process, output data consists of a virtual pixel, whose size is about 4 × 4 of the original pixel. Data from two rows enable the milli-seconds confirmation (the time difference is about 87ms). In addition, sampling timing and binning group of pixels are chosen such that the virtual pixels cover a staggered grid of the sky (Figure 2). Image strips of 64 × 306 virtual pixels from the first sampling row and those of 63 × 306 virtual pixels from the second sampling row for each band are the basic unit of the data.

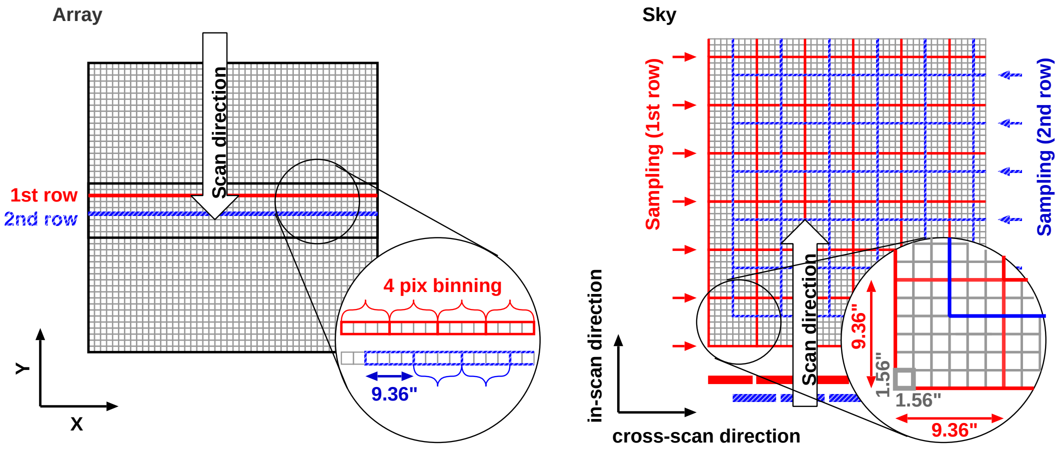

Figure 2: (Left) Illustration of the nest 4×4 mode array operation in the survey mode. (Right) Virtual pixel alignment : Red lines show virtual pixels from the first sampling row, blue lines show virtual pixels from the second sampling row, and gray lines show the final output pixels after the data reduction processes.

2 Outline of data processing

Figure 3 shows the flow of the data processing. First, we extract the IRC All Sky Survey data from the packets and reformat into FITS image format data. Each FITS file contains on chip integrating data within an interval of resets for each band. From this data, image strips are generated after removal of instrumental anomaly effects. Each image strip has a field of view of 10' × 40' corresponding to the scan area. There are two frames corresponding to two detector rows used by scan observations for each band. Point-like sources are extracted using the source extractor (SExtractor: Bertin & Arnouts 1996). A region with connected pixels above 3 sigma threshold is a candidate. The two frames are combined into one frame with one sixth virtual pixel size. From the combined frame, point-like sources are extracted again using SExtractor. At this time, a region connected at least 32 pixels above 3 sigma threshold is a candidate. Then we have point source candidates from row #1 data (candidate1), candidates from row #2 data (candidate2), and candidates from combined frame (candidate3). Candidate3 are the basic entries of our source list and each candidate is confirmed examining entries in candidate1 and candidate2. This confirmation is the so called 'milli-seconds confirmation' where the time shift is only 87 ms. The valid observed area is marked with the same pixel size as the combined image. This called a Norb map, which means number of observations. Point-like sources are listed in the event list and used as one of the input data for the pointing reconstruction process. After the pointing reconstruction process, all events have reconstructed position data. Then, fluxes of the point source events are calibrated. In parallel, WCS (world coordinate system) of Norb maps are adjusted by the result of the pointing reconstruction. From the calibrated point source event list and Norb maps, point source catalogue is generated.

In this version, reset anomaly and linearity corrections limit the accuracy. Errors in these corrections limit the repeatability of the detected source flux.

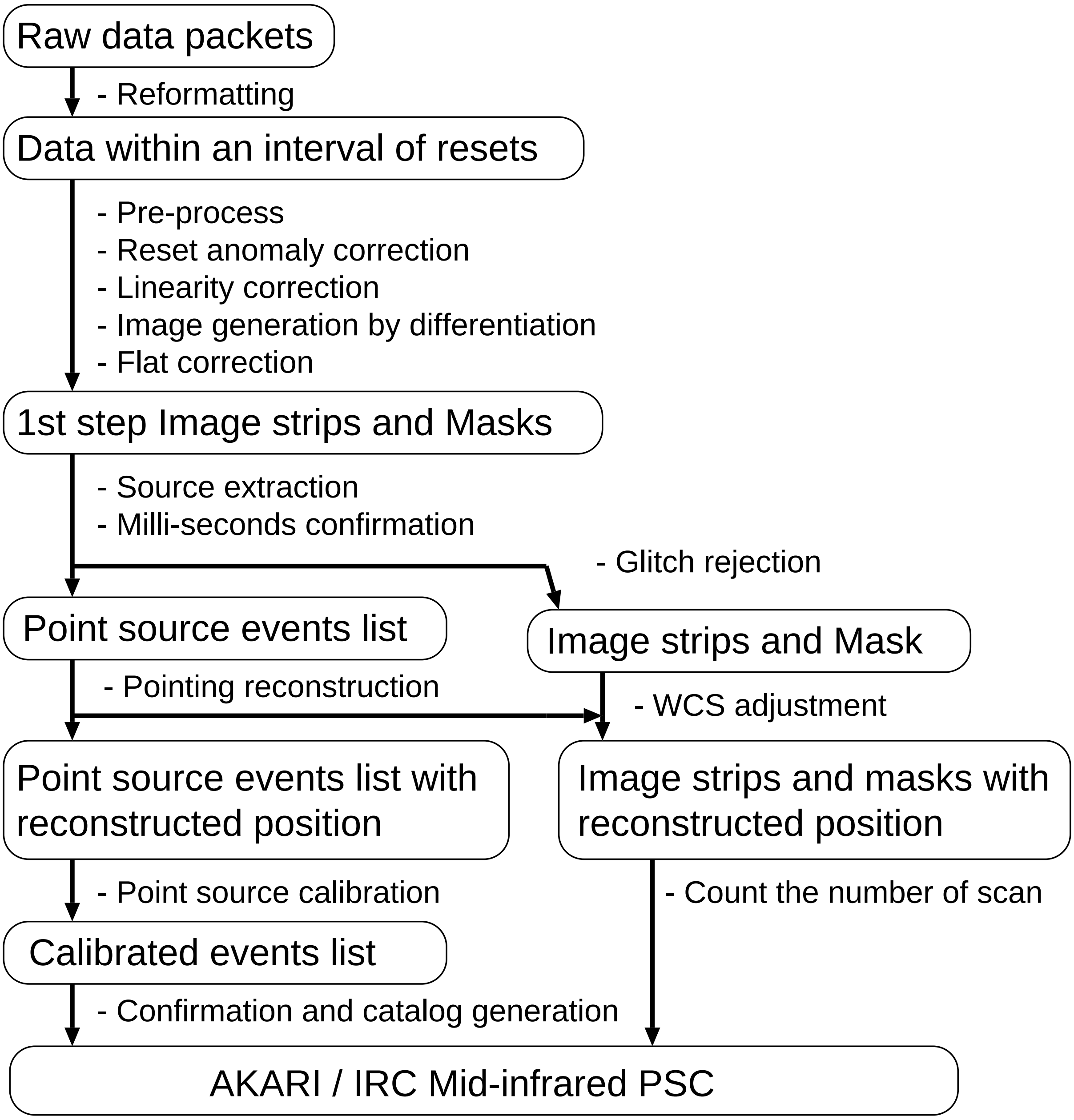

Figure 3: Data processing flow

3 Pointing reconstruction

The pointing reconstruction, that is the determination of the scan position during the survey, is carried out as follows. Information of satellite attitude determined by the onboard computer is stored in the AOCS telemetry, together with the data from the AOCS sensors. The Groundbase Attitude Determination System (G-ADS) works with these data. Onboard ADS and G-ADS data are similar to each other, as they are based on the same sensor data, however, G-ADS processing is more carefully done and should be more reliable.

The remaining major source of uncertainty is the alignment between the AOCS system and the telescope axis, and its time variation. This is solved by the pointing reconstruction processing. The AKARI team in the ESA's European Space Astronomy Centre (ESAC) is in charge of this processing. Input data are G-ADS attitude, ephemeris data, Focal-plane Star Sensor (FSTS) scan data, the IRC All-Sky Survey point source event list, and input reference catalogues. The output returned from the processing are survey attitude information and identification list of the IRC event. The latter contains positions of all events in the input list, and is used for generating the AKARI/IRC PSC.

Two input reference catalogues are generated for AKARI pointing reconstruction: (i) the near-infrared FSTS Reference Catalogue, and (ii) the mid-infrared IRC Reference Catalogue. FSTS Reference Catalogue has a total of 2,862,152 sources brighter than the 10th magnitude in the J-band in the 2MASS Point Source Catalogue. 1,327,581 sources were cross-matched against the Tycho-2 astrometric catalogue to improve the astrometric information. The IRC Reference Catalogue is composed by: (i) the whole MSX Infrared Astrometric Catalogue; (ii) the whole MSX Point Source Catalogue; and (iii) sources detected by IRAS for which a clear counter part exists in the 2MASS Point Source Catalogue at high galactic latitudes. The total number of entries is 670,833.

The Pointing Reconstruction software *PRESA* provides the transformation between the G-ADS and the Focal Plane attitude. The combination of a forward and a backward continuous-discrete Kalman filter is used to estimate the transformation quaternion from G-ADS to the Focal Plane attitude.

Figure 4 demonstrates the pointing reconstruction performance. The plot shows the fraction of the IRC events with error smaller than the given values. The error is the distance between the positions determined from the pointing reconstruction results and those from the position reference catalogue. For fair evaluation, the pointing reconstruction for this test was carried out using randomly selected sources amounting to half of the catalogue, then the positions of the sources from the other half catalogue are determined for the evaluation. The error includes pointing reconstruction processing error and the measurement error. For the brightest sources the measurement error should have minor contribution, and we can conclude that the position accuracy is better than three arcsec in 95 per cent of the events (c.f., original requirement was 3 and 5 arcsec in the in- and cross-scan direction in the final version).

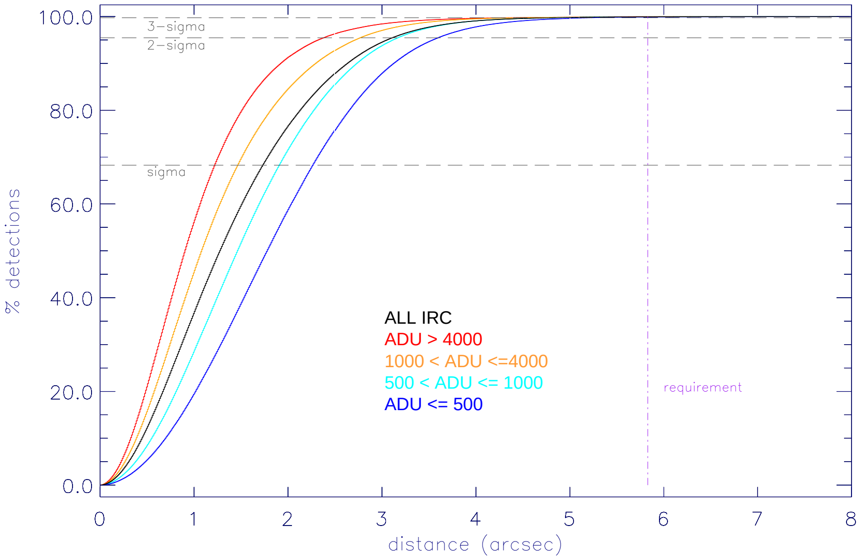

Figure 4: Statistical error of the pointing reconstruction using 50% of the catalogue data. The error for events in remaining 50% data is defined as the distance between the position determined by pointing reconstruction and the position of the input reference catalogue. The lines show the fraction of the IRC events with an error smaller than given values. Color of lines denotes the flux range of events.

4 Flux calibration

Standard stars for the absolute flux calibration were selected from standard stars in Cohen et al. (1999), those in the ecliptic pole regions (Cohen et al. 1996, 1999, 2003a, 2003b; Cohen 2003), those in the LMC (Meixner et al. 2006; Cohen et al. 2003b), and those for the calibration of ISO (Cohen et al. 1995). The flux ranges of the stars in Cohen et al. (1999) are 5 – 200 Jy and 1 – 40 Jy in the S9W and L18W bands, respectively. Standard stars in the North and South Ecliptic Pole (NEP and SEP) regions and LMC/SMC regions that are established by M. Cohen for the calibration of the Spitzer/IRAC are also used for faint-end calibration. The flux ranges of these stars are 0.01 – 1 Jy and 0.003 – 0.3 Jy in the S9W and L18W bands, respectively. Several bright standard stars established by M. Cohen for the calibration of ISO instruments are also used for bright-end calibration. The flux ranges of these stars are 75 – 520 Jy and 17 – 280 Jy in the S9W and L18W bands, respectively. We identify the events whose position offsets are less than 5 arcsec for the input standard stars and obtain their output ADUs. We disregard data that are obviously mis-identified judging from fluxes.

The in-band flux density of each band at the effective wavelength, $f_\lambda^{quoted}(\lambda)$ is calculated by the following equation:

$$f_\lambda^{quoted}(\lambda_i) \quad = \quad \frac{\int_{\lambda_{is}}^{\lambda_{ie}} R_i(\lambda)\lambda f_\lambda(\lambda)d\lambda}{\int_{\lambda_{is}}^{\lambda_{ie}} (\frac{\lambda_i}{\lambda})R_i(\lambda)\lambda d\lambda} \tag{1}$$

where $f_\lambda(\lambda)$ is the flux density of a standard star SED (Cohen template) and $R_i(\lambda)$ is the spectral response function (the transmission of the optics and the response of the detector, unit: electron·photon^{-1}) of the band i. Here $f_\lambda \propto \lambda^{-1}$ is assumed. This is the convention adopted by IRAS, COBE, ISO, Spitzer/IRAC, and AKARI IRC pointing observation (Tanabé et al. 2008). The adopted effective wavelengths of each band, λ_i are listed in Table 2 along with the range of the integration (λ_{is}, λ_{ie}).

Table 2: The effective wavelengths λ_i and the range of the integration,λ_{is}, and λ_{ie}

band	λ_i	λ_{is}	λ_{ie}
S9W	9.00	2.50	23.510
L18W	18.00	2.58	28.720

The relations between pipeline output ADUs of events and calculated in-band fluxes of the standard stars are shown in Figures 5 and 6 for the S9W and L18W bands. The relations are nearly linear but we can see systematic difference from the linear relation (bottom right panels in the figures) which suggest that the flux conversion should be made with non-linear functions.

We assume a conversion function as a linear function in log-log scale;

$$\ln(\mathrm{Flux}) \quad = \quad \sum_i a_i(\ln(\mathrm{ADU}))^i \tag{2}$$

i.e

$$\mathrm{Flux} \quad = \quad \exp\left(\sum_{i=0}^{2} a_i(\ln(\mathrm{ADU}))^i\right) \tag{3}$$

where Flux denotes flux in Jy unit and ADU denotes output digital counts from the pipeline. The coefficients of the function were derived from least square fitting between pipeline output ADUs and calculated in-band fluxes of the standard stars. Derived coefficients for S9W and L18W are shown in Table 3.

Table 3: Coefficients of the conversion function for S9W and L18W

band	a_2	a_1	a_0
S9W	0.00850918	0.806013	-7.66656
L18W	0.00717589	0.829091	-7.35238

The best-fit functions are shown in Figures 5 and 6. The deviations of the fluxes converted with the derived conversion functions are shown in the bottom panel of the figures. The deviations seems flat and the fluxes converted with the derived functions reproduce satisfactorily the in-band fluxes. We adopt these functions as conversion functions for the point sources. But we should note that the conversion functions are applicable for the point sources whose fluxes are up to 500 Jy in the S9W band and up to 300 Jy in the L18W band because of the limits in the calibration standard.

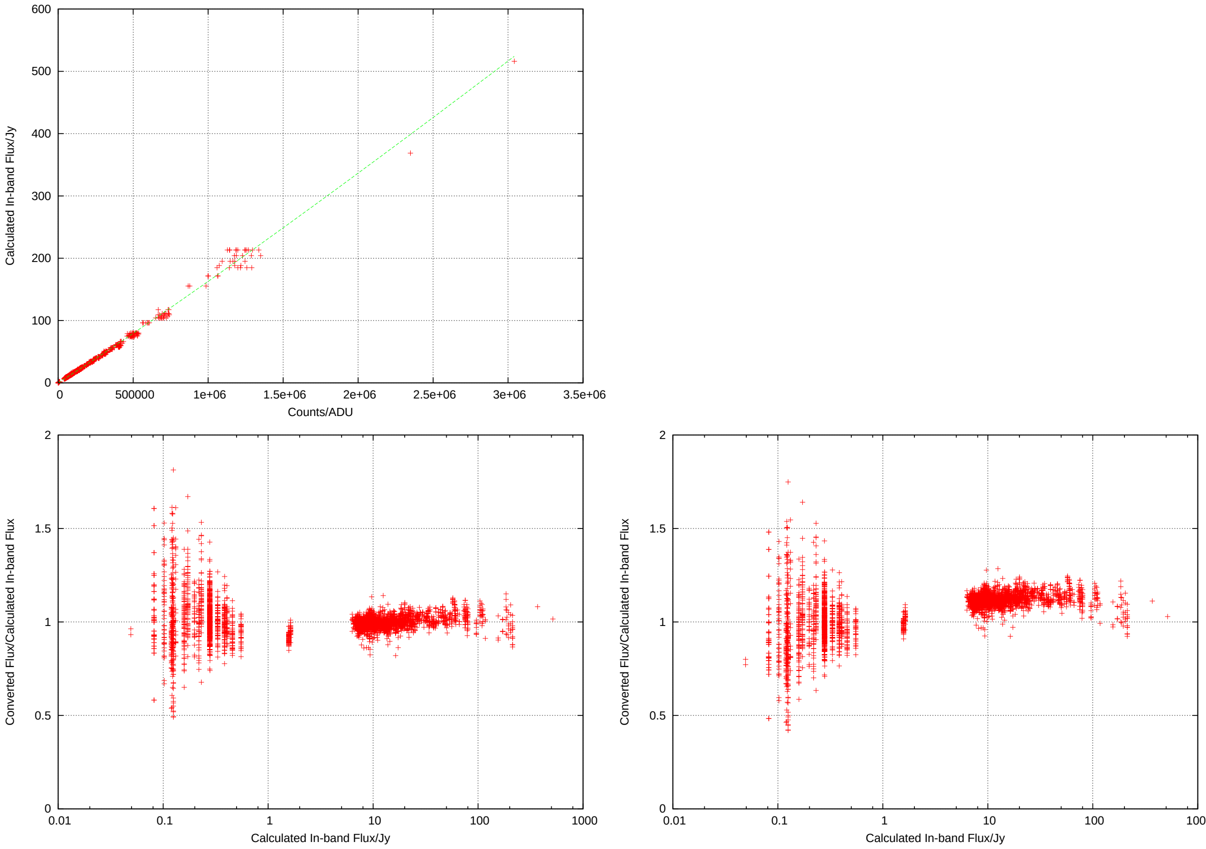

Figure 5: Top: The pipeline output ADUs of events is plotted as a function of the calculated in-band fluxes of the standard stars in the S9W band. Derived non-linear conversion function for S9W band are over plotted. Bottom left: The deviations of the ratio of calibrated fluxes with the non-linear conversion function over model fluxes of the standard stars. Bottom right: The deviations of the same as left but linear conversion function is assumed.

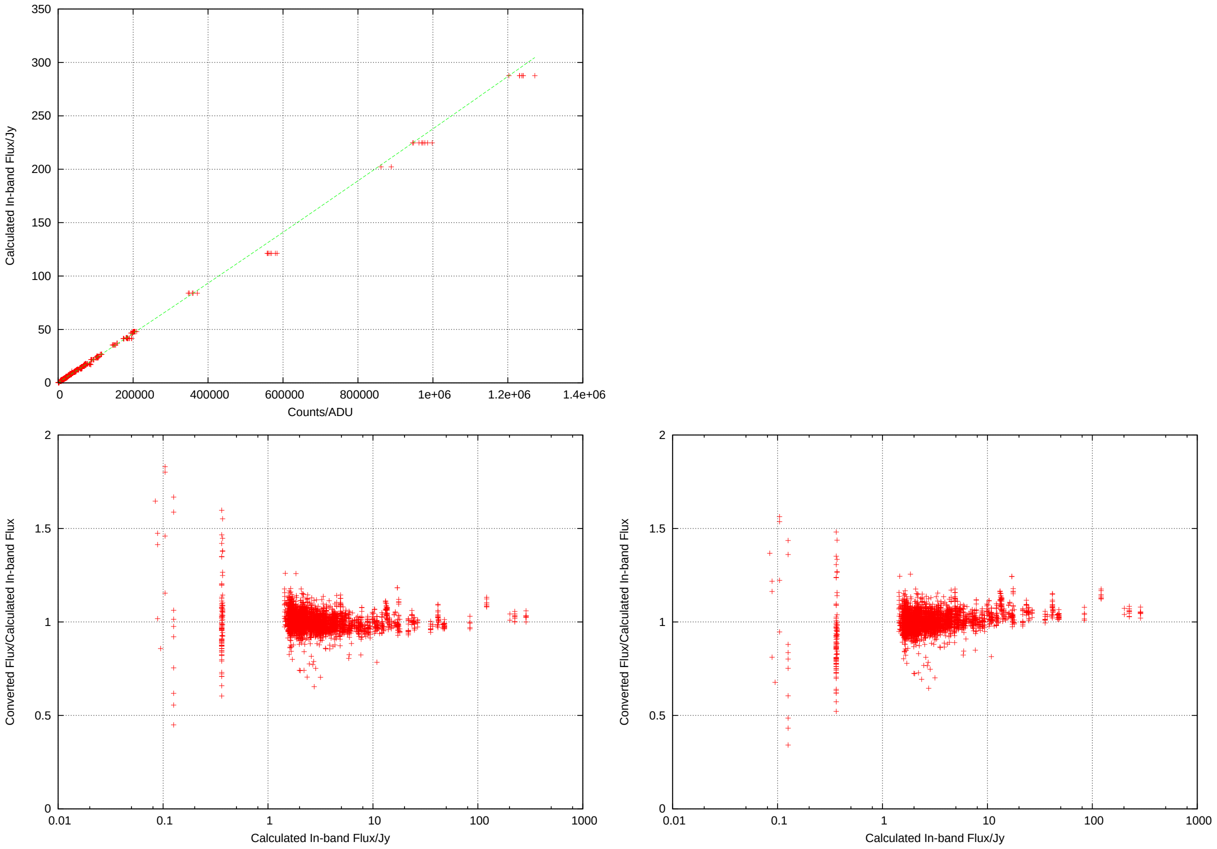

Figure 6: Top: The pipeline output ADUs of events is plotted as a function of the calculated in-band fluxes of the standard stars in the L18W band. Derived non-linear conversion function for L18W band are over plotted. Bottom: The deviations of the ratio of calibrated fluxes with the non-linear conversion function over model fluxes of the standard stars. Bottom right: The deviations of the same as left but linear conversion function is assumed.

To test the long-term stability of the photo response we investigated five standard stars that have been observed more than 30 times during the time of the survey. Figure 7 shows the ratio of the fluxes of individual measurements to the average fluxes of these stars as a function of time. From these data we deduce that the sensitivity is stable at the ∼2% level during the entire period of the observations.

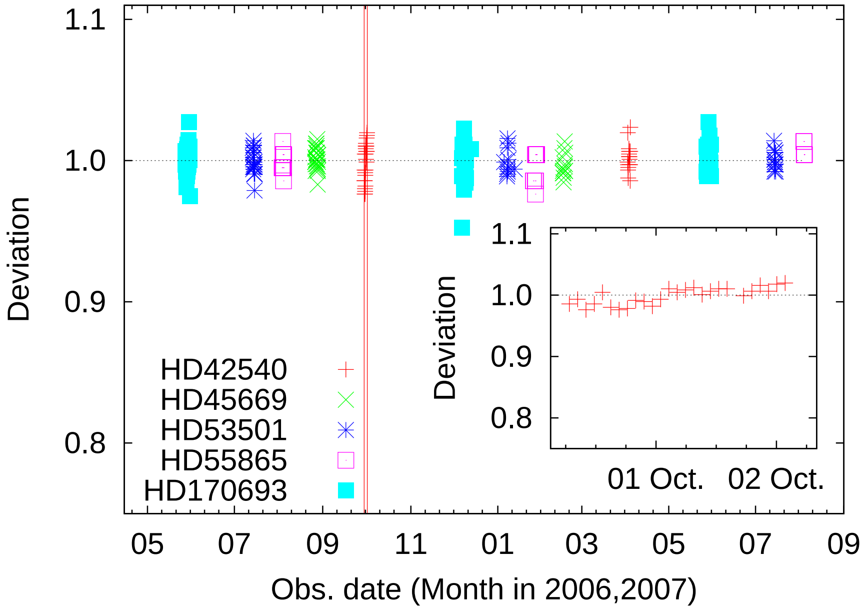

Figure 7: Ratio of the measured fluxes to the average fluxes as a function of observing time for five bright (>1 Jy) standard stars observed at 9 μm more than 30 times during the survey. The stars used and the corresponding 9 μm fluxes and number of detections are: HD42540 (plus, 8.33 Jy, 44 times), HD45669 (cross, 9.79 Jy, 43 times), HD53501 (star, 9.30 Jy, 45 times), HD55865 (open box, 16.7 Jy, 33 times) and HD170693 (filled box, 9.60 Jy, 76 times), respectively. The closeup shown in the right bottom panel is to check for the temporal variation on a short timescale.

Laboratory measurements of the filter transmission indicate possible blue leaks between the 3 μm and 4 μm for the 9 μm band and between the 6 μm and 7 μm for the 18 μm band. They are 0.01% at maximum and much smaller than the measurement errors. Thus the presence of the blue leaks is not confirmed. We calculated the predicted fluxes of the standard stars with and without the blue leak and confirmed that the difference is less than 0.1%. We have verified that the blue leak of the 18 μm band is negligible (< 1%) compared to the systematic errors by using asteroid calibrators whose flux can be well predicted (Müller & Hasegawa, private communication).

5 Catalogue generation

In the position calibrated events list, a group of events whose positions are within a threshold value is recognized as a source. In this "grouping" process, radius of 5 arcsec is employed as a threshold value. Events affected by the South Atlantic Anomaly (SAA) have been excluded in this process. Grouping was done in the S9W band and in the L18W band independently. After the first grouping process, distance from a source candidate to the nearest one is checked and if there are more than two groups within 7 arcsec, we consider them as a single source with some outskirt events. In this case we take the group with maximum number of events as a source candidate and discard other groups. Then, the source list in the S9W band and that in the L18W band are merged into one list. Sources within 7 arcsec are treated as the same source in both band. Position (RA, DEC) and position error (POSERRMJ, POSERRMI, POSERRPA: see section 6) are calculated from events in the S9W band only, if the number of available data is larger than or equal to 2. Otherwise, these data are calculated from events in the L18W band only. We do not merge position data from two bands. Flux of each event is calibrated from the value of FLUX_AUTO, measured by SExtractor (see SExtractor v2.5 user's manual) as described in section 4. Flux in the catalogue is calculated as a mean value of that of each event. Event data near the edge of the image strips are excluded from flux calculation with exceptional case that there is only one or zero events available. This exceptional case is notified by FLAGS09 and FLAGS18 entry of the catalogue. The mean values of fluxes and associated errors (standard deviations of the mean) are defined as:

$$< X > \;=\; \mathrm{MEAN} = \frac{\sum_i^N X_i}{N} \tag{4}$$

$$< \sigma > \;=\; \mathrm{ERROR} = \sqrt{\frac{\sum_i^N (X_i - < X >)^2}{N(N-1)}} = \frac{\mathrm{r.m.s.}}{\sqrt{N}} \tag{5}$$

where N is the number of data.

6 Catalogue contents and format

The contents of the current version AKARI/IRC PSC are summarized in Table 4. The catalogue will be distributed in two ways: a FITS file and access via DARTS database query. DARTS interface will be provided later. The current version does not include complete information. The contents and format are carefully defined for permanent use, but we do not rule out the possibility of future updates according to the user's feedback or technical progresses.

Table 4: Contents of the AKARI/IRC Point Source Catalogue

Name	Type	Format	Column	Description
OBJID	int32	I10	1 – 10	AKARI source ID number.
OBJNAME	string	15A	11 – 25	AKARI source name. The format is HHMMSSS+/-DDMMSS
RA	double	F10.5	26 – 35	Right Ascension (J2000)[deg]
DEC	double	F10.5	36 – 45	Declination (J2000)[deg]
POSERRMJ	float	F8.2	46 – 53	Major axis of position error ellipse [arcsec]
POSERRMI	float	F8.2	54 – 61	Minor axis of position error ellipse [arcsec]
POSERRPA	float	F8.2	62 – 69	Position angle of Major axis [deg]
FLUX09	float	E11.3	70 – 80	Flux density in S9W [Jy]
FLUX18	float	E11.3	81 – 91	Flux density in L18W [Jy]
FERR09	float	E10.2	92 – 101	Flux error in S9W [Jy]
FERR18	float	E10.2	102 – 111	Flux error in L18W [Jy]
FQUAL09	int16	I2	112 – 113	Flux quality flag for S9W
FQUAL18	int16	I2	114 – 115	Flux quality flag for L18W
FLAGS09	int16	Z5	116 – 120	Bit flags data quality for S9W. 1: not month confirmed, 2: (not used in this version), 4: (not used in this version), 8: use edge
FLAGS18	int16	Z5	121 – 125	Bit flags data quality for L18W. 1: not month confirmed, 2: (not used in this version), 4: (not used in this version), 8: use edge
NSCANC09	int16	I5	126 – 130	Number of scans in which the source is detected for S9W
NSCANC18	int16	I5	131 – 135	Number of scans in which the source is detected for L18W
NSCANP09	int16	I5	136 – 140	Total number of scans that possibly observed the source for S9W
NSCANP18	int16	I5	141 – 145	Total number of scans that possibly observed the source for L18W
MCONF09	int16	I3	146 – 148	1 is month confirmed and 0 is not. Inverted value of 1st bit of FLAGS09
MCONF18	int16	I3	149 – 151	1 is month confirmed and 0 is not. Inverted value of 1st bit of FLAGS18
NDENS09	int16	I4	152 – 155	Number of sources in 45 arcsec radius for S9W
NDENS18	int16	I4	156 – 159	Number of sources in 45 arcsec radius for L18W
EXTENDED09	int16	I3	160 – 162	Extended source flag
EXTENDED18	int16	I3	163 – 165	Extended source flag
MEAN_AB09	float	F8.2	166 – 173	The average of major and minor axes of source extent for S9W [arcsec]
MEAN_AB18	float	F8.2	174 – 181	The average of major and minor axes of source extent for L18W [arcsec]
NDATA_POS	int16	I5	182 – 186	Number of events which are used for positional calculation
NDATA09	int16	I5	187 – 191	Total number of events that contribute to the measurements for FLUX09
NDATA18	int16	I5	192 – 196	Total number of events that contribute to the measurements for FLUX18

Description

OBJID

Source ID number.

OBJNAME

Source name from its J2000 coordinates, following the IAU Recommendations for Nomenclature (2006). The format is HHMMSSS±DDMMSS, e.g., 0123456+765432 for a source at (01h23m45.6s, +76d54m32s). The source must be referred to in the literatures by its full name: AKARI-IRC-V1 J0123456+765432, where V1 refers to the version code.

RA, DEC

J2000 Right Ascension and Declination of the source position in degree.

POSERRMJ, POSERRMI, POSERRPA

One-sigma error of the source position expressed by an ellipse with Major and Minor axes [arcsec], and Position Angle [deg; East from North]. If only two events are available, POSERRMJ is calculated from the distance of the two events and POSERRMI is set to the same as POSERRMJ.

FLUX09, FLUX18

Flux density of the source in the two IRC bands in Jansky.

FERR09, FERR18

Flux error in the two IRC bands. Errors are defined as equation 5.

FQUAL09, FQUAL18

Flux density quality flag in the two IRC bands. 3 when flux is valid and 0 when flux is not available.

FLAGS09, FLAGS18

Bit flags of data quality:

1(LSB): not month confirmed

This means that the period between the first detection and the last detection is shorter than a month.

2: saturated (not used in this version)

4: use SAA (not used in this version)

8(MSB): use edge events

If the number of events is too small, we use the event data near the edge of the image strip. In this case, this flag warn you of underestimation of the flux.

NSCANC09, NSCANC18

Number of scans on which the source is detected. Normally, NSCANC is less or equal to NSCANP. In some exceptional case, resultant position of the source drops out from the image stripe boundary and NSCANC is larger than NSCANP.

NSCANP09, NSCANP18

The number of times the source position has been scanned during the survey.

MCONF09, MCONF18

1 is month confirmed and 0 is not. Inverted value of LSB of FLAGSxx.

NDENS09, NDENS18

The number of sources in 45 arcsec radius.

EXTENDED09, EXTENDED18

The flag indicates that the source is possibly more extended than the point spread function. This is "TRUE" when MEAN_AB > 15.6 [arcsec]

MEAN_AB09, MEAN_AB18

The average of radius along major and minor axes of images, i.e. $(< a > + < b >)/2$ where $< a >$ and $< b >$ are the mean semi-major and semi-minor axis lengths of images estimated by SExtractor.

NDATA_POS

Number of events used to calculate the mean coordinates. If the source has more than two available S9W events, the position is estimated from S9W events only, else the position is estimated from L18W events, i.e.
NDATA_POS = NSCANC09 for NSCANC09 ≥ 2
NDATA_POS = NSCANC18 for NSCANC09 < 2

NDATA09, NDATA18

Number of events that contribute to the flux measurements in the two bands. Normally, events near the edge of the image strip are excluded from the measurements. Note that if only 0 or 1 event are available, the flux is computed also from edge events.

7 Performance

7.1 Number of sources

The AKARI/IRC Point Source Catalogue contains 870,973 sources, out of which 844,649 are detected in the S9W band and 194,551 in the L18W band. Observations exist in both bands for 168,227sources. As shown in Table 5, by far the largest fraction of sources is detected in the flux range 0.1 to 1 Jy (73% at S9W and 76 % at L18W).

Events affected by the South Atlantic Anomaly (SAA) are excluded from the catalogue.

Table 5: Number(N) of detected sources as a function of flux level

Range Jy	N (S9W)	N (L18W)
0 – 0.1	146,817	1,317
0.1 – 1	619,561	148,675
1 – 10	71,254	39,321
10 – 100	6,580	4,750
100 – 1000	444	478
> 1000	2	10
total	844,649	194,551

Table 6: Number of cross matches of the AKARI/IRC PSC with 2MASS sources.

Survey	Number of Sources	Search radius	Matching Sources
2MASS	2862152	$3''$	716021

Table 6 provides the results of a cross correlation between the AKARI/IRC PSC and the 2MASS survey. For the 2MASS catalogue, the search has been limited to magnitude J = 10.

7.2 Extended sources

Figure 8 shows the dependence of MEAN_AB on flux. This figure provides the possibility of distinguishing between two populations of sources: extended and point sources. In this version of the catalogue, extended sources are defined as those with MEAN_AB ≥ 15.6 [arcsec], and the associated EXTENDED flag is set to unity. This flag is based on a fixed threshold value. We note, however, that also bright point source might appear as extended. The histogram in Figure 9 shows clearly that the distribution of these parameters is dominated by point sources.

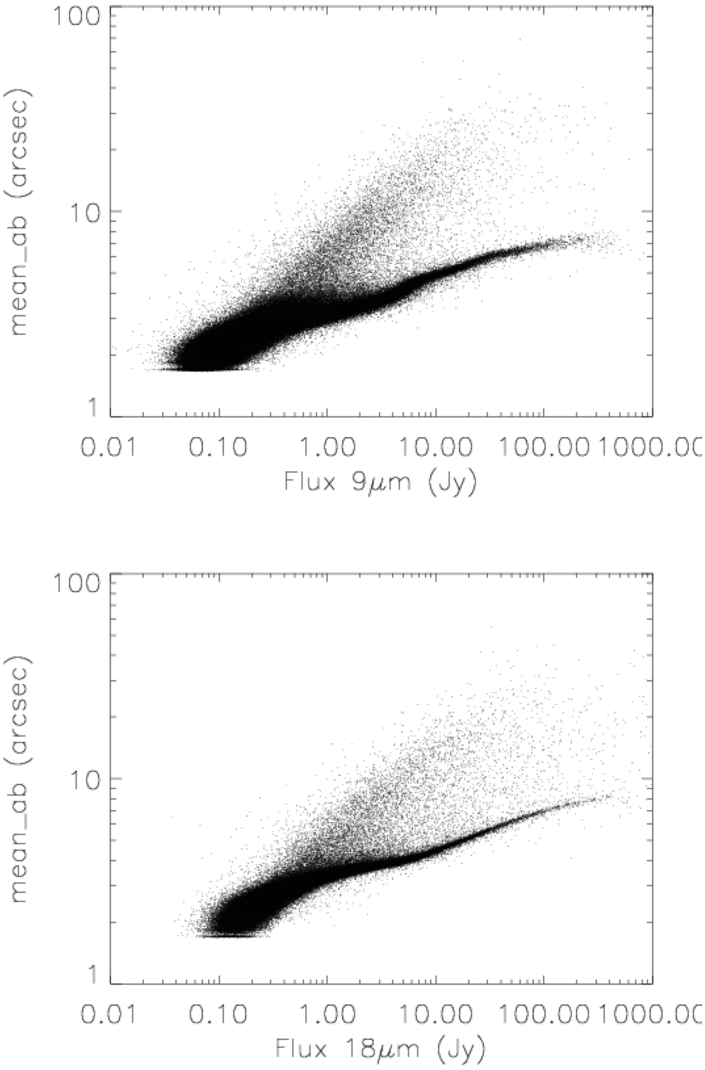

Figure 8: MEAN_AB as a function of the S9W (top) and L18W (bottom) flux.

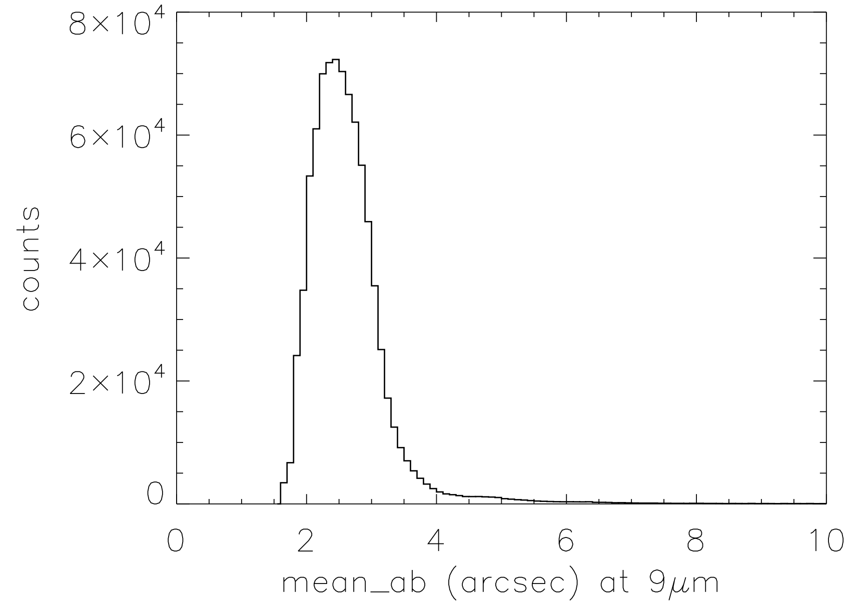

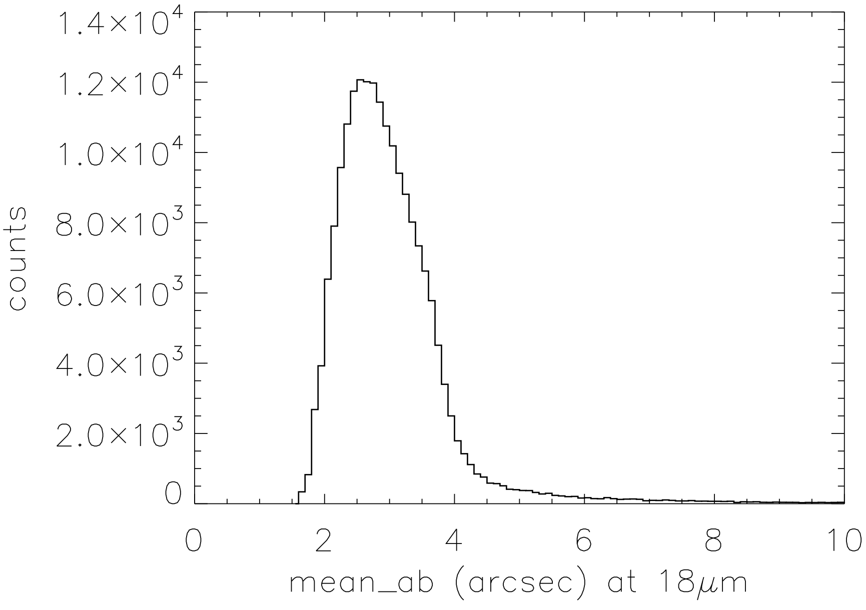

Figure 9: Histogram of MEAN_AB for S9W (top) and L18W (bottom).

7.3 Accuracy of coordinates

For a given source, the distribution of the repeatability errors on coordinates can be described as an error ellipse, whose minor and major axis are defined as the observed minimum and maximum standard deviation of the distribution, and the position angle is that of the major axis. A test of the internal accuracy of AKARI coordinates is given Figure 10, showing the minor axis of the error ellipse as a function of that of the major axis. One can easily appreciate that the errors cluster around $0.2''$–$0.3''$.

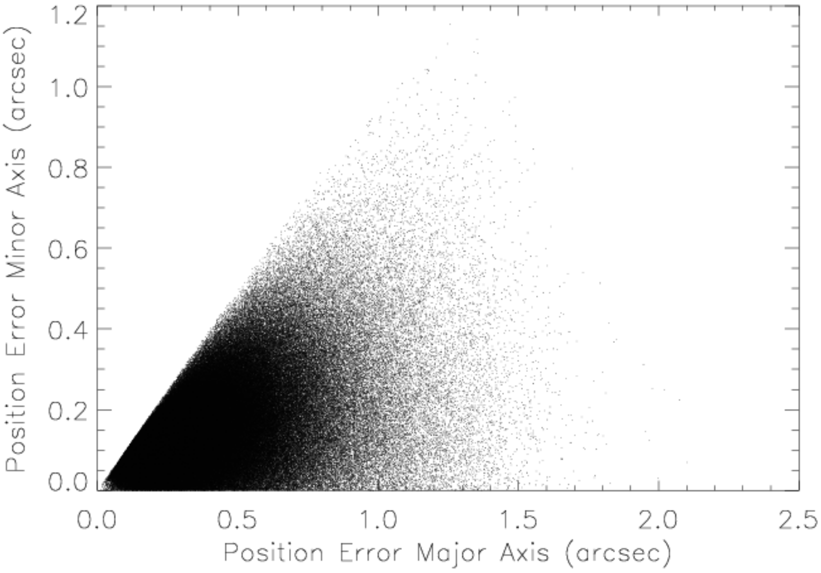

Figure 10: Position repeatability. Sources used in this plot has more than two events. Radius size of error ellipsoid estimated from the positions of events attributed the same object is plotted as a point.

We have tested the accuracy of coordinates of the AKARI/IRC PSC sources through a cross-match with the the 2MASS survey. Figure 11 show the number AKARI/IRC PSC sources matching with the 2MASS J, H and K survey as a function of the seach radius. While too many sources remain unmatched for the case of search radius is $1''$, there is no substantial gain by increasing it above $3''$, a value that is adopted in the following.

Figure 12 shows the histogram of the angular separation between the AKARI/IRC PSC coordinates and the 2MASS reference coordinates for cross matched sources. According to these data, nearly 95% of the sources have an angular separation $\leq 2''$, while about 73 % have a separation $\leq 1''$. The mean angular separation between AKARI and 2MASS coordinates of the same sources is 0.765 ± 0.574 arcsec. Larger internal errors are of course expected for fainter sources, as shown in Figure 13.

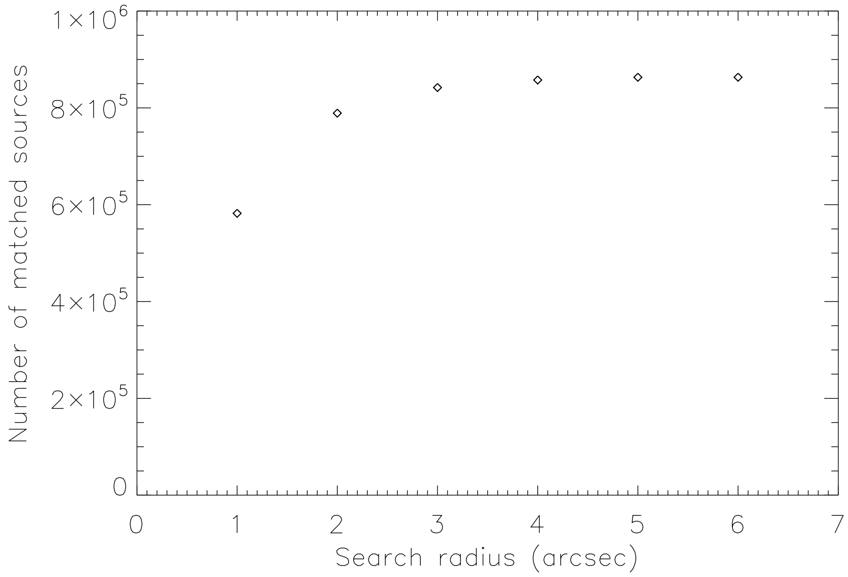

Figure 11: Number of AKARI/IRC PSC sources matching the 2MASS catalogue as a function of search radius.

7.4 Flux Accuracy

There are basically two ways to assess the flux accuracy. The first consists of a repeatability test in which the internal accuracy of fluxes is measured through the rms errors on mean fluxes for sources observed more than once. The second, after applying the flux calibration, consists in comparing flux-calibrated photometry with the known fluxes of standard stars.

Figure 14 shows the relative errors (FERR09/FLUX09 and FERR18/FLUX18) as a function of flux for all sources with positive flux. As expected, larger errors are seen at lower flux levels. However, the probability of observing large errors is rather small, as shown in the histograms in Figure 15. The figure shows indeed that for the most probable error is around 2 – 3 %. For about 80 % of the data the relative errors are smaller than 15%, and for about 96% are smaller than 30%. At this stage, we cannot quantify how variable objects artificially contribute to increase the scatter on observed fluxes.

The data in Figure 15 can be used also to compute the typical Signal-to-Noise ratio (S/N) to be associated with different flux levels. This is done in Figure 16, which shows S/N as a function of the flux. The figure indicates that for the faintest sources with $\sim$ 0.045 Jy in the S9W band, the expected S/N is $\sim$ 6, while it is $\sim$ 3 for $\sim$ 0.06 Jy in the L18W band. The figure shows as well that S/N increases with increasing flux and then from flux above 0.6Jy / 0.9Jy S/N become constant or slightly decrease at $\sim$ 20 / $\sim$ 15 for S9W / L18W respectively. These S/N limitation comes from the accuracy limits in the data reduction process. Errors in the correction of detector reset anomaly, linearity, and individual sensitivity of pixel cause the fluctuation of the detection flux and limits the repeatability of the flux measurements.

The flux calibration and linearity correction applied on event list data are described in section 4. Here, Figure 17 provides a test of the accuracy of the flux-calibrated data after the catalogue generation in the two MIR bands. The full dynamical range of the MIR detectors cannot be fully explored with the standard stars that have been used, especially with respect to linearity properties. In any case, the overall performance in terms of linearity and self-consistency is good: in the flux

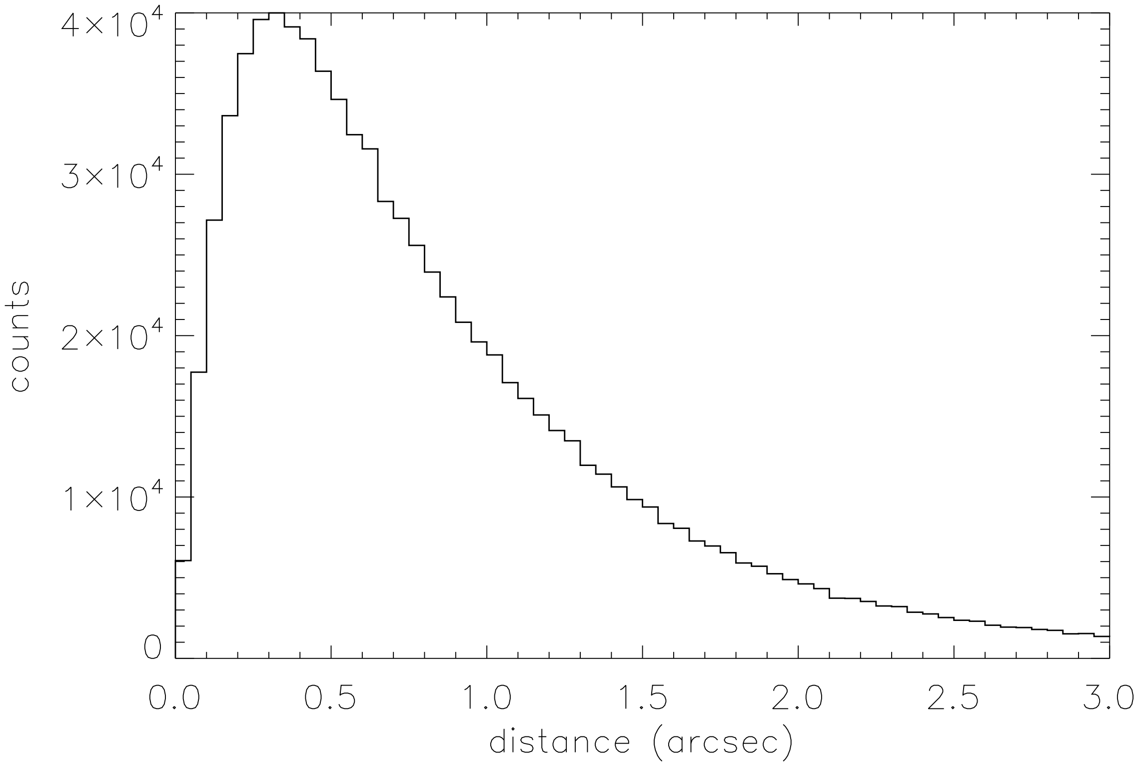

Figure 12: Histogram of the angular separation between AKARI PSC coordinates and the 2MASS coordinates for the common sources.

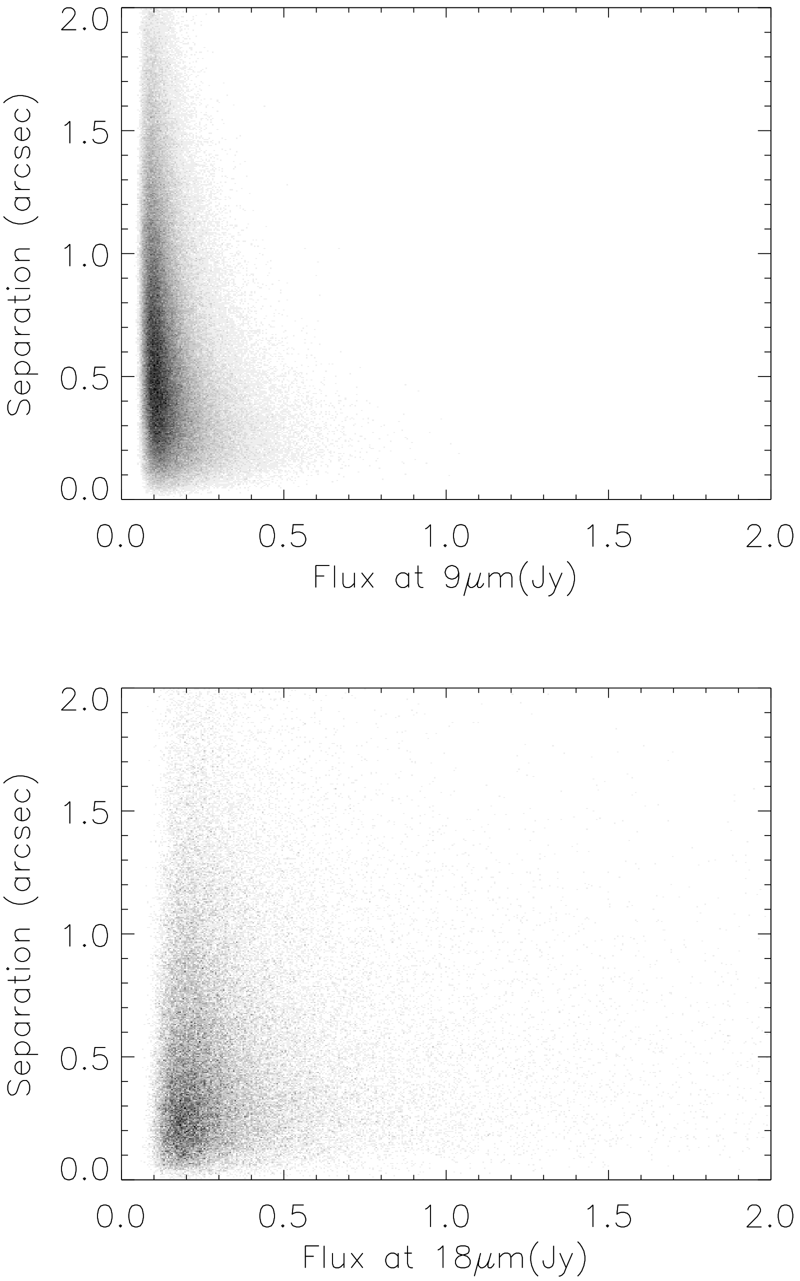

Figure 13: Angular separation between AKARI PSC coordinates and the 2MASS coordinates as a function of flux.

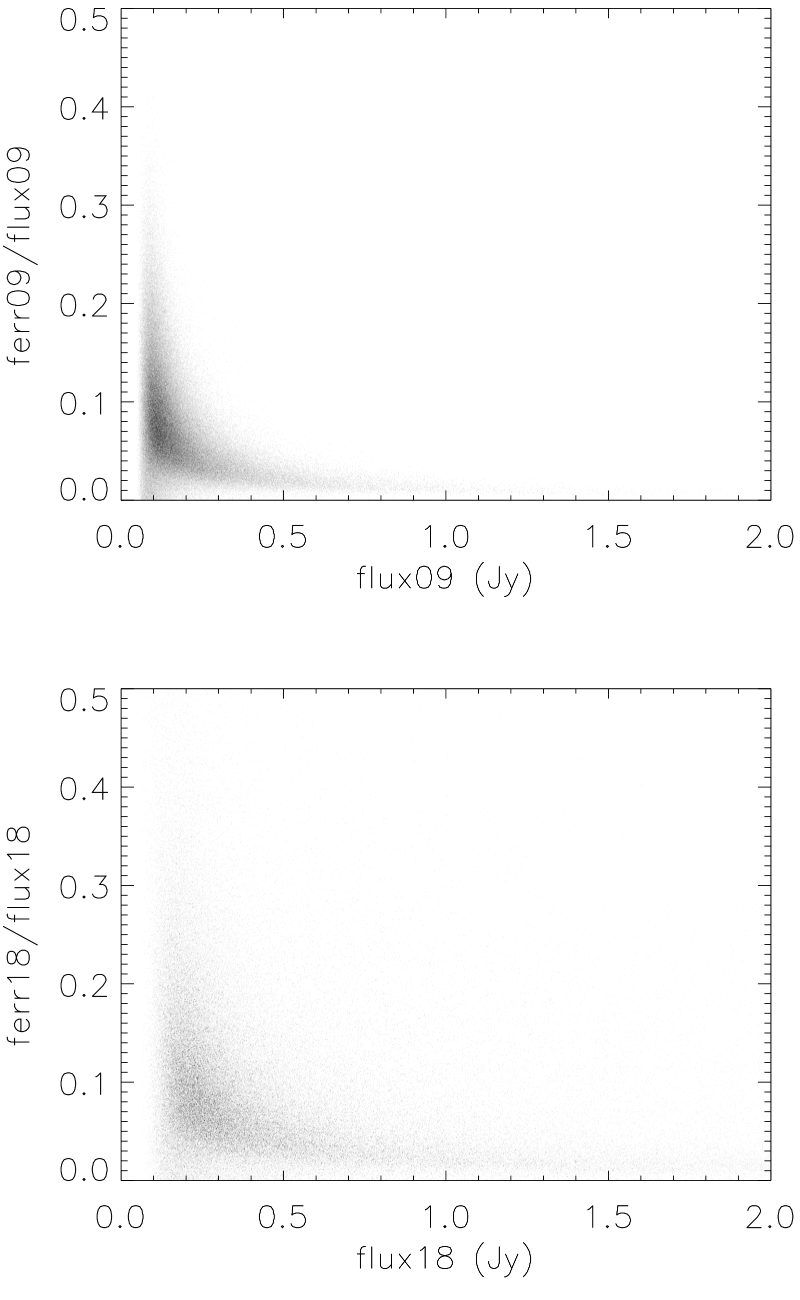

Figure 14: Internal relative errors on the S9W and L18W fluxes as a function of flux.

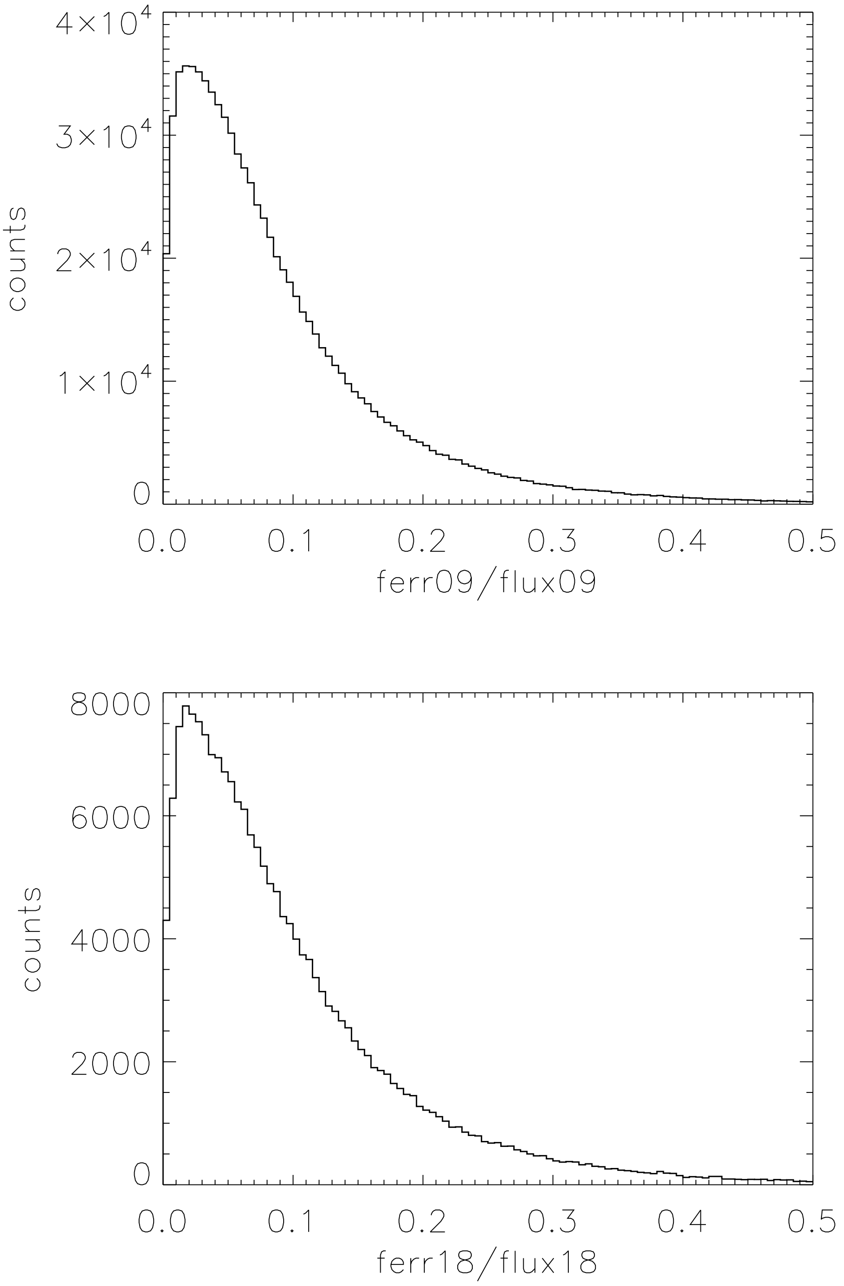

Figure 15: Histograms showing the distribution of internal relative error on the S9W and L18W band fluxes as a function of flux.

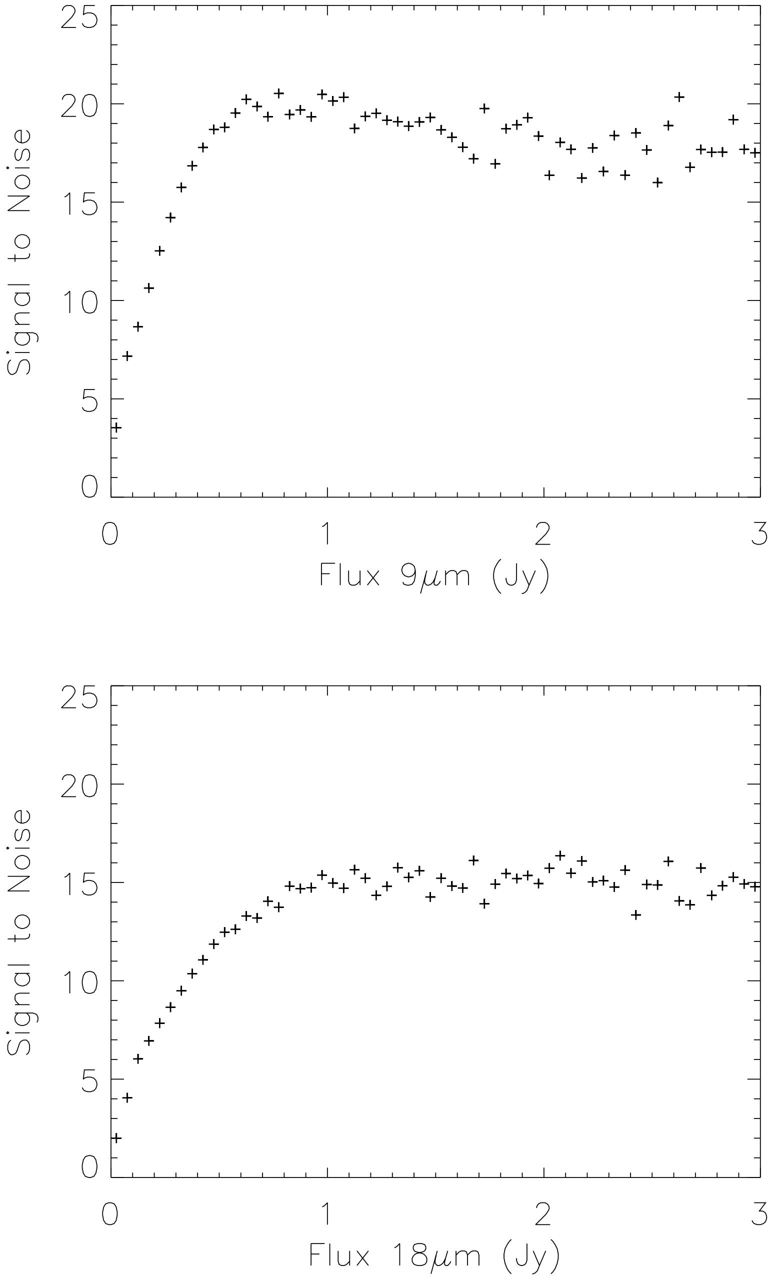

Figure 16: Signal to Noise ratio as a function of the S9W and L18W flux.

range explored we find: $F_\nu^{AKARI}/F_\nu^{Standard} = 0.970 \pm 0.070$(rms) at S9W from 412 measurements, and $F_\nu^{AKARI}/F_\nu^{Standard} = 1.001 \pm 0.045$(rms) at L18W from 406 measurements.

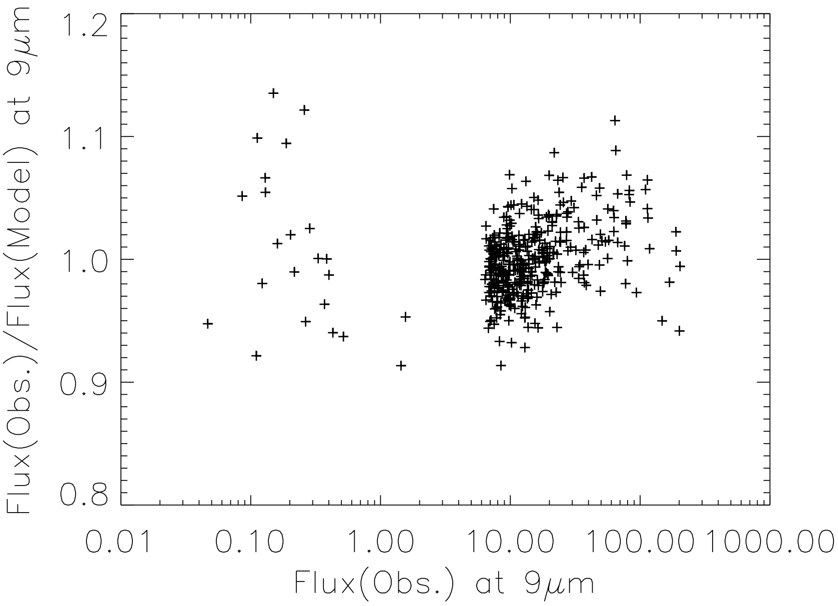

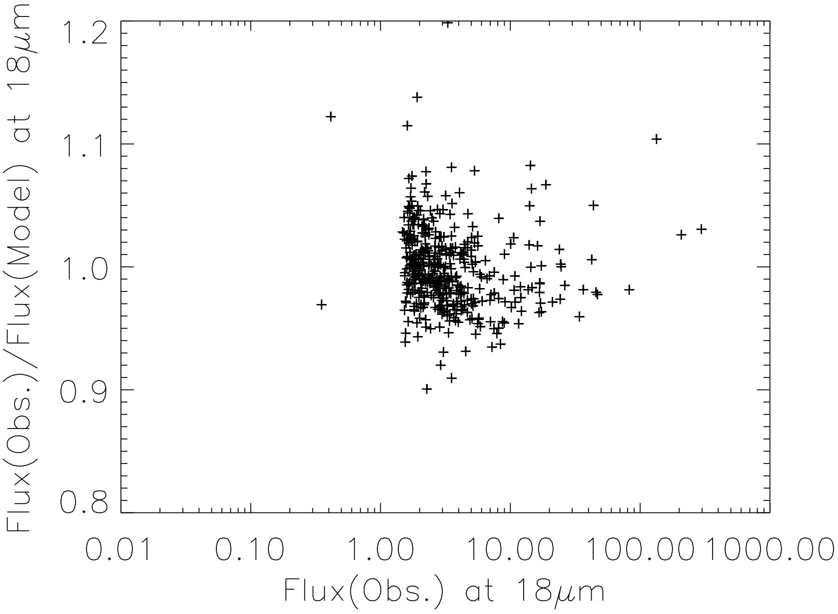

Figure 17: Flux ratio of AKARI/MODEL in the S9W and L18W bands. MODEL flux is calculated in-band flux of standard stars and AKARI flux is FLUX09 or FLUX18 in the catalogue. Note that FLUX09 and FLUX18 is the mean value of events fluxes, whereas Figure 5 and 6 use the fluxes of events.

7.5 Sky coverage

Figure 18 shows the histogram of sky coverage by the MIR-S channel and MIR-L channel. More than 96/97 % of the whole sky are observed twice or more in S9W/L18W band respectively.

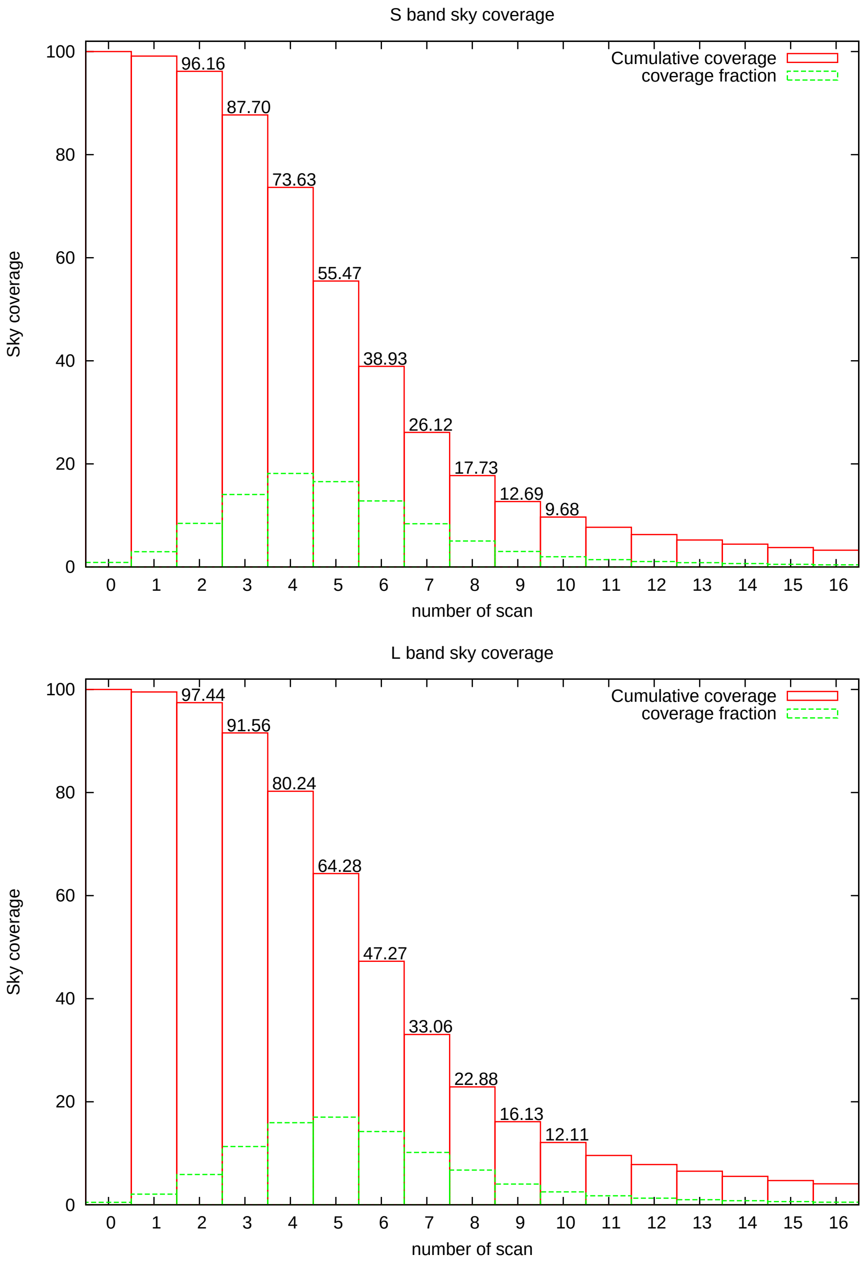

Figure 18: The sky coverage and cumulative coverage area in percent as a function of number of scan for S9W (top) and for L18W (bottom).

7.6 Completeness

The completeness of a survey above a given flux level, is usually defined as the fraction of true sources that can be detected above that level. It is difficult to apply this concept to the AKARI survey because one should dispose of a statistically significant sample of true sources with known IRC fluxes. The standard stars used for the AKARI/IRC PSC calibration might not represent a statistically significant sample, also in view of the rather poor coverage at low flux levels.

To assess the completeness of the AKARI-MIR survey we have thus taken a different approach, based on the distribution of sources according to their flux. Figure 19 shows the histogram of AKARI MIR sources in the S9W and L18W bands with a similar histogram for the IRAS PSC sources. This histograms show an interesting feature: source counts decline exponentially after a peak value is reached around 0.1 Jy (S9W) and 0.2 Jy (L18W). This is better seen in Figure 20, where the following regressions lines have been over plotted to the data:

$$\log(N) = 2.89 - 1.97\log(\mathrm{Flux09})$$

$$\log(N) = 2.59 - 1.77\log(\mathrm{Flux18})$$

One can thus make the reasonable assumption that the exponential decay is an intrinsic property of source counts at the relevant wavelengths and, on this basis, one can define completeness as the ratio of the number of sources actually observed by the number of sources predicted by the above equations. The results of completeness are shown in Figure 21. From this figure we deduce the completeness rations reported in Table 7. [†]

Table 7: Completeness and Signal-to-Noise ratio

		S9W		
Completeness	5%	50%	80%	100%
Flux[Jy]	0.06	0.09	0.12	0.20
S/N	6.0	7.9	8.5	11.3
		L18W		
Completeness	5%	50%	80%	100%
Flux[Jy]	0.10	0.17	0.22	0.30
S/N	5.0	6.8	8.0	9.0

To evaluate the detection limit of the survey, we can make use of the AKARI/IRC PSC Signal-to-Noise characteristics shown in Figure 16. From this figure one can deduce that, for S/N $\sim$ 5, the detection limit is about 0.05 and 0.09 Jy in the S9W and L18W bands, respectively.

A summary of the completeness of the survey at various flux levels, together with the corresponding values of the Signal-to-Noise ratio are given in the Table 7. These results are in fairly good agreement with Ishihara et al. (2006, 2008).

[†] Values are slightly different from Ishihara 2010 which based on the previous version of the catalogue.

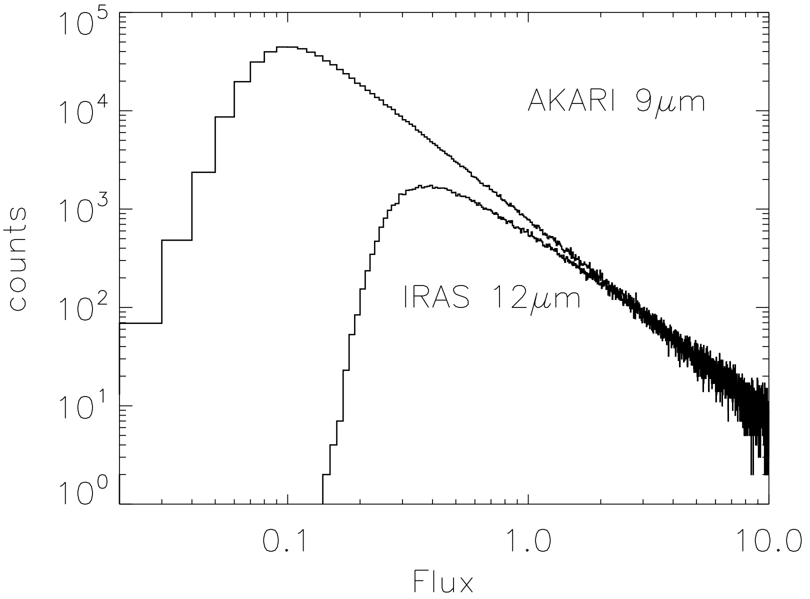

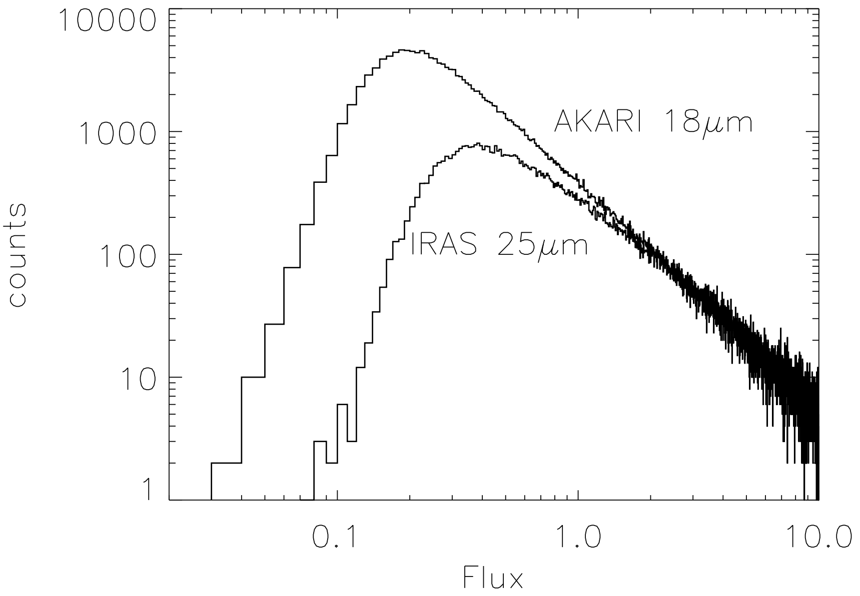

Figure 19: The distribution of sources as a function of the S9W and L18W flux for AKARI/IRC PSC is compared with that from the IRAS survey at 12 μm and 25 μm in log-log scale.

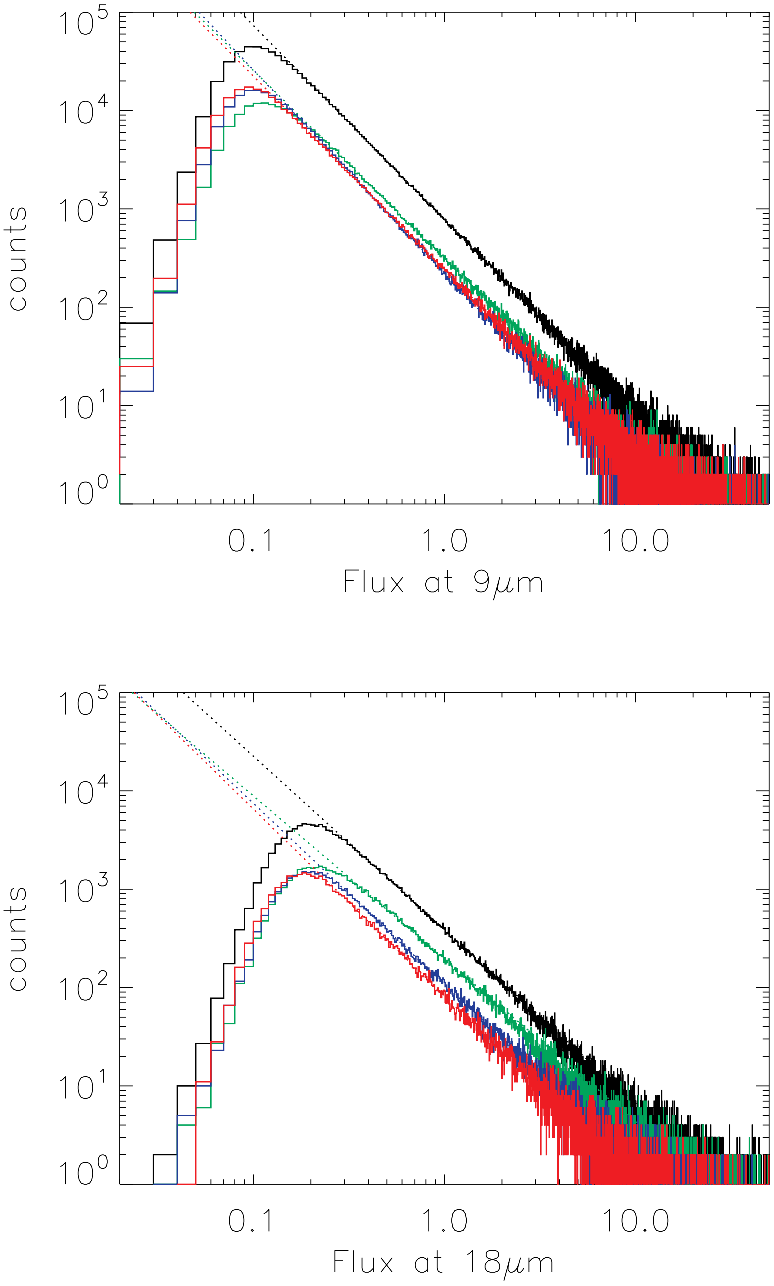

Figure 20: The distribution of sources as a function of the S9W and L18W flux for AKARI/IRC PSC. The over plotted dash-dotted line is a fit to the source counts for fluxes above the peak of the distribution. Plot in black shows the distribution of all sources in the catalogue, and plots are made also for galactic latitudes, $|b| < 2.2°$ (green), $2.2° < |b| < 8.3°$ (blue), and $|b| > 8.3°$ (red), separately.

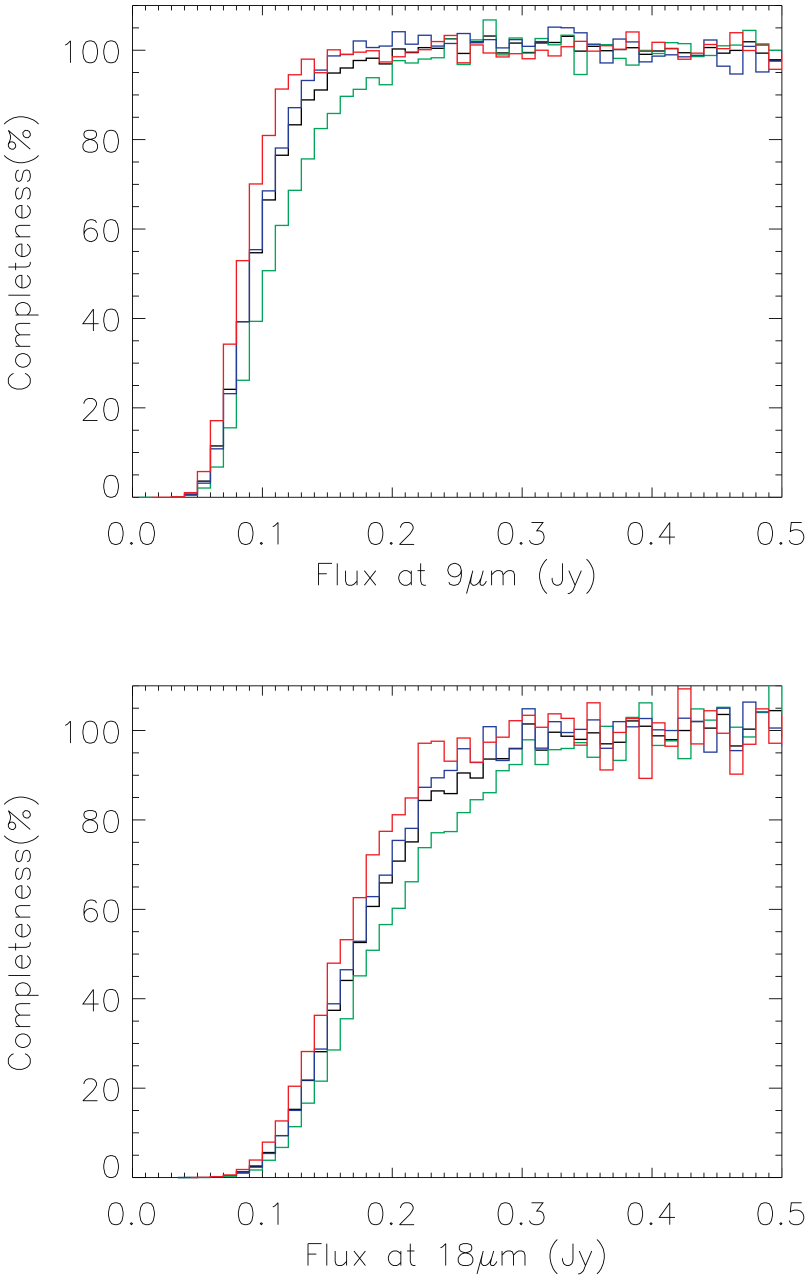

Figure 21: Completeness ratio of the AKARI/IRC survey in the S9W and L18W bands. Plot in black shows the ratio for whole sky, and plots are made also for galactic latitudes, $|b| < 2.2°$ (green), $2.2° < |b| < 8.3°$ (blue), and $|b| > 8.3°$ (red), separately.

REFERENCES

Bertin, E., and Arnouts, S., 1996 A&AS 317, 393
Bertin, E. SExtractor v 2.5 User's manual
Beichman, C. A., Neugebauer, G., Habing, H. J., Clegg, P. E., & Chester, T. J. 1988, Infrared astronomical satellite (IRAS) catalogs and atlases, Explanatory supplem ent, 1
Cohen, M., et al. 1992 AJ, 104, 1650
Cohen, M., et al. 1995 AJ, 110, 275
Cohen, M., et al. 1996 AJ, 112, 2274
Cohen, M., et al. 1999 AJ 117, 1864
Cohen, M., et al. 2003a AJ, 125, 2645
Cohen, M., et al. 2003b AJ, 126, 1090
Cohen, M. 2003 in Proc. The Calibration Legacy to the ISO Mission, ESA SP-481, 135
IAU Recommendations for Nomenclaturer, Version 2006 November 28, *http://cdsweb.u-strasbg.fr/iau-spec.html*
Ishihara, D., et al., 2006 PASP 118, 324
Ishihara, D., et al., 2008 SPIE 7010, 70100B-1
Ishihara, D., et al., 2010 A&Ap accepted
Kawada, M., et al., 2007 PASJ 59, S389
Lorente, R., et al. AKARI IRC Data User Manual version 1.4 2008
Murakami, H., et al., 2007 PASJ 59, S369
Onaka, T., et al., 2007 PASJ 59, S401
Tanabé, T., et al., 2008 PASJ 60, S375

Changes from beta version

- In the milli-seconds confirmation process, we ruled out fake detections more strictly than beta 1 version. As a result, number of catalogued source is reduced.
- Number of scan is counted for each source.
- Number of scan map is generated and we can estimate have sky coverage.
- Format of the catalogue is changed.
  OBJECTID → OBJID
  NAME → OBJNAME
  FVARxx → removed